NANO LETTERS

Letter

pubs.acs.org/NanoLett

Segmentally Structured Disk Triboelectric Nanogenerator for Harvesting Rotational Mechanical Energy

Long Lin,[†] Sihong Wang,[†] Yannan Xie,[†] Qingshen Jing,[†] Simiao Niu,[†] Youfan Hu,[†] and Zhong Lin Wang*[,†,‡]

[†]School of Materials Science and Engineering, Georgia Institute of Technology, Atlanta, Georgia 30332-0245, United States

[‡]Beijing Institute of Nanoenergy and Nanosystems, Chinese Academy of Sciences, Beijing, China

Supporting Information

ABSTRACT: We introduce an innovative design of a disk triboelectric nanogenerator (TENG) with segmental structures for harvesting rotational mechanical energy. Based on a cyclic in-plane charge separation between the segments that have distinct triboelectric polarities, the disk TENG generates electricity with unique characteristics, which have been studied by conjunction of experimental results with finite element calculations. The role played by the segmentation number is studied for maximizing output. A distinct relationship between the rotation speed and the electrical output has been thoroughly investigated, which not only shows power enhancement at high speed but also illuminates its potential application as a self-powered angular speed sensor. Owing to the nonintermittent and ultrafast rotation-induced charge transfer, the disk TENG has been demonstrated as an efficient power source for instantaneously or even continuously driving electronic devices and/or charging an energy storage unit. This work presents a novel working mode of TENGs and opens up many potential applications of nanogenerators for harvesting even large-scale energy.

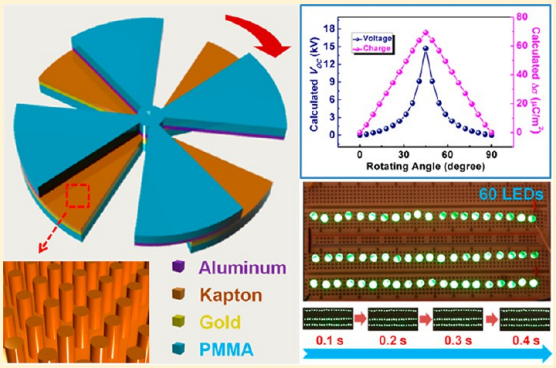

KEYWORDS: *Triboelectric nanogenerator, in-plane charge separation, self-powered system, angular speed sensor*

Scavenging mechanical energy from ambient environment has attracted increasing interest not only for achieving self-powered systems, but also for large-scale energy needs.[1−4] Various approaches for harvesting mechanical energy have been developed that are based on piezoelectrics,[5−9] electromagnetics,[10,11] and electrostatics,[12,13] and so forth. The recently invented triboelectric nanogenerator (TENG)[14−20] provides an effective approach to convert mechanical energy into electricity, based on the coupling between triboelectrification[21−23] and electrostatic induction. The output performance of the TENG highly relies on the effectiveness of the charge separation process.[17,19] In previous works, the separation of triboelectric charges was along the normal direction in reference to the triboelectric-charged surfaces (tribo-surfaces), which was accomplished relying on the resilience of the device structure when the external force was withdrawn. However, such approaches might lead to high processing cost and difficulty for fully packaging the TENG device. Moreover, the vertical separation based TENG may only work for low-frequency mechanical triggering, such as impact and deformation. Recently, we have introduced a contact-sliding based approach for TENG,[24,25] in which the two tribo-surfaces are in contact. A time-dependent change in their contact area results in a lateral polarization of the triboelectric charges (tribo-charges) parallel to the tribo-surfaces, which can also give high power output.

Here in this work, we developed a segmentally patterned disk-shaped TENG, in which a periodic overlapping and separation process of the two groups of sectors on the two concentric and closely contacted disks is achieved by relative rotation. This design not only introduces the sliding triboelectrification between the two contacting surfaces of the sectors but also facilitates a rotation-induced periodic, in-plane charge separation for electricity generation. This in-plane charge-separation-based working mechanism was demonstrated with the combination of numerical calculations and experiments. With this rotation-based TENG, both finer segmentations and larger rotation speed lead to a faster charge transfer between the electrodes through an external circuit, producing a large current output at a high frequency (117.6 μA and 29.0 mA/cm^2 of 66.7 Hz at a rotating speed of 1000 rpm). Owing to its high output current and large frequency, multiple light-emitting diodes (LEDs) were lit up continuously, and a power storage unit such as a capacitor was quickly charged. The disk TENG is an important progress toward the practical application of nanogenerators and self-powered systems.

Received: April 11, 2013
Revised: April 30, 2013
Published: May 8, 2013

The basic structure of the disk TENG is composed of two disk-shaped components with four sectors each, as schematically illustrated in Figure 1a. In the fabrication of the TENG

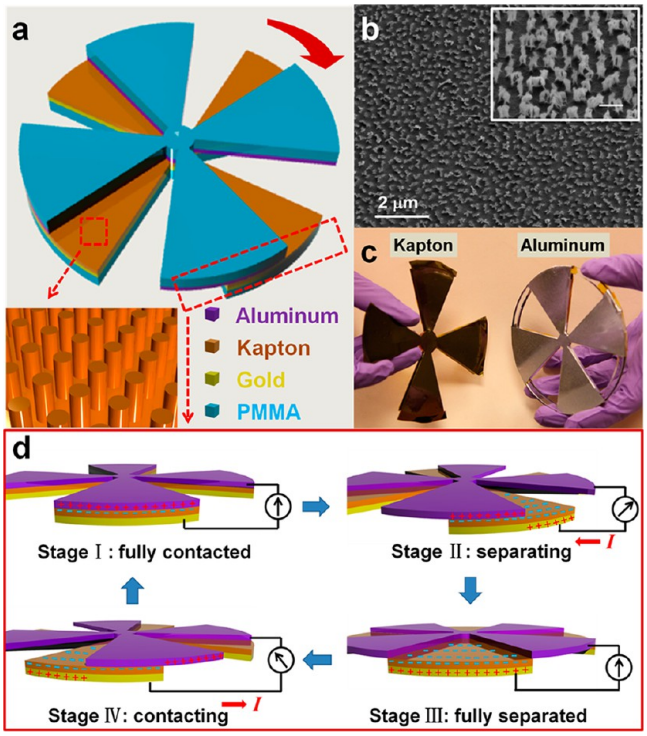

Figure 1. Basic structure and proposed working principle of the disk TENG. (a) A schematic illustration showing the structure design of the disk TENG. The inset (bottom left) is an enlarged figure showing the Kapton nanorod array created on the surface area. (b) A top-view SEM image of the Kapton nanorods showing its uniformity in a large range. The inset is a high magnification SEM image of the Kapton nanorods in 30°-tilted view. The scale bar is 500 nm. (c) A photograph showing the two parts of a real disk TENG. (d) Schematic illustrations showing the proposed working principle of the disk TENG with the electrons flow diagram in four consecutive stages within a full cycle of electricity generation. Please note that only one pair of sectors (the cross-section area entangled in part a) was shown with surface charges for clarity of illustration, and the surface charges on the interface area between Al foil and Kapton film are hidden and are not drawn for easy presentation.

device, two poly(methyl methacrylate) (PMMA) sheets were first processed by laser cutting to form the desired four-sector-structured cyclostyle that served as the templates for the effective contacting parts of the TENG. Then, a 50-μm-thick Kapton film with Au electrode deposited on the back side was manually patterned into this exact shape and then securely attached onto one of the templates, while a piece of Al foil tailored into the same shape was attached on the other template. The Al part and Kapton part was brought to a face-to-face intimate contact and the Al part was driven to spin on the surface of the Kapton around their common axis. To promote the triboelectrification and increase the effective contact area between the two layers, a Kapton nanorod (NR) array was created on the Kapton surface by a top-down approach[26] through inductive coupled plasma (ICP) reactive ion etching, as displayed in the inset of Figure 1a. Scanning electron microscopy (SEM) images of the Kapton NRs are shown in Figure 1b. After a two-minute ICP etching, the NRs were uniformly distributed on the surface of Kapton, with an average diameter and length of 150 and 600 nm, respectively. The length of the NRs increases with the etching time (Figure S1). Figure 1c is a photograph of the two parts of the disk-shaped TENG with a diameter of 4 in. The total effective area of the TENG device is 40.54 cm^2.

The disk TENG in this work presents a different working mode from the vertical contact-separation based configuration. The working principle of the disk TENG is based on the triboelectrification and the relative-rotation-induced cyclic in-plane charge separation between Al and Kapton, as shown in Figure 1d. In the relative rotation, the Al surface and Kapton surface slide one relative to the other, so that the electrons will be injected from the Al foil to the inner surface of the Kapton film, leaving net positive charges on the Al foil and net negative charges on the Kapton film. The electricity generation process of the disk TENG can be divided into four stages: in Stage I, the two disks are at an overlapping position. Since the two charged surfaces are closely contacted with no polarization, there will be no potential difference between the two electrodes, thus no current flow in the external load. When the Al foil rotates in reference to the Kapton film, the corresponding two segments start to have a partially mismatched contact area (Stage II), and the in-plane tribo-charges are thus separated in the direction almost parallel to the sliding direction, which will induce a higher potential on the Al layer than the Kapton's electrode; thus the electrons in the electrode attached to the Kapton film will be driven to flow to the Al foil through an external load (forming a current flow in the reverse direction), so that an opposite potential is generated to balance the potential difference created by the separated tribo-charges. In this process, the electrons keep flowing until the two disks reach fully mismatch in the contacting segmented areas (e.g., for 45° of rotation in this case), which is represented by Stage III. At this moment, both the induced potential difference and the amount of transferred charges between the two electrodes reach the maximum values. In Stage IV as the top plate continues spinning, the Kapton surface begins to get contacted with another adjacent sector of Al foil, and the potential difference between two electrodes will drop with the decrease of the mismatch area. As a result, the electrons will flow back in the opposite direction from the Al foil to the electrode attached to the Kapton film. Thus, the entire process will result in an alternating-current (AC) output. Such a charge transfer cycle will start over from Stage I when the two plates reach a complete overlapping again.

To gain a more quantitative understanding of the proposed working principle of the disk TENG, we employed finite element simulation to calculate the potential difference between the two electrodes and the transferred charge density at consecutive stages in a full cycle of charge transfer. The triboelectric charge density on the inner surface of Kapton film and Al foil was assigned as 75 μC/m^2. Figure 2a shows the calculation results in the four stages with rotation angles of 0° (Stage I), 22.5° (Stage II), 45° (Stage III), and 67.5° (Stage IV), respectively. In Stage I, the two layers are in full contact with each other, and there is no potential difference or charge transfer. Subsequently, as the top plate spins across this position, introducing the charge separation in the lateral direction, both the potential difference and the density of transferred charges between the Al foil and the Kapton's electrode will build up, via 1.62 kV and 34.5 μC/m^2 at 22.5° of half separation (Stage II), and finally to the peak values of 14.71

dx.doi.org/10.1021/nl4013002 | Nano Lett. 2013, 13, 2916−2923

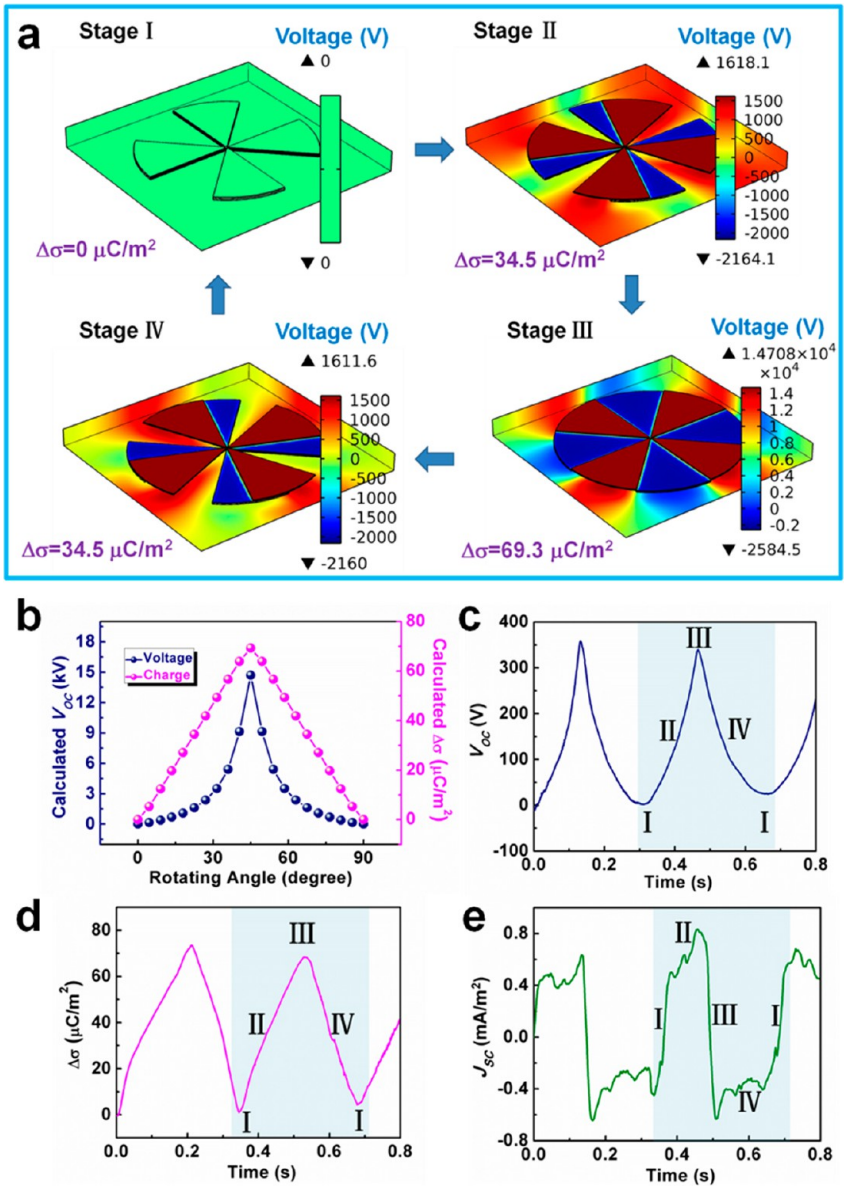

Figure 2. Numerical calculations of the charge transfer process of the disk TENG. (a) The numerical calculation of the potential difference and transferred charge density between two electrodes in four different stages within a full cycle of rotational motion: (I) fully contact, (II) half separated, (III) fully separated, and (IV) half contact. (b) A summary of the calculated open-circuit voltage and transferred charge density in a full cycle of rotation. The calculation takes place from the 0° position to the 90° position, and the step angle is 4.5°. (c–e) The measured (c) open-circuit voltage, (d) transferred charge density, and (e) short-circuit current density in a full cycle of rotational motion at 45 rpm.

kV and 69.3 μC/m^2 at the fully separated position of 45° (Stage III). In the second half of this cycle (Stage IV), both the potential difference and transferred charge density decrease as the contact area begins to recover, and they show a symmetric behavior at the angle of 67.5° compared with Stage II.

The calculated potential difference and transferred charge density in a full cycle (from the 0° position to the 90° position with the step angle of 4.5°) were depicted in Figure 2b. It can be observed that the transferred charge density displays a linear relationship with the rotating angle in each of the half cycles, while the potential difference presents a sharper peak, with an elevated slope around the fully separated position (the rotating angle of 45°). Assuming a constant value of triboelectric charge density (σ_0) and uniform distribution of these charges on the inner surface of Al and Kapton, the amount of transferred charges should ideally equal to the amount of separated charges, which is proportional to the separated area (ΔA, for one sector). Therefore, the transferred charge density ($\Delta\sigma$) has the following relationship with the rotating angle ($\Delta\theta$):

$$\frac{\Delta\sigma}{\sigma_0} = \frac{\Delta A}{A_0} = \frac{(1/2)\Delta\theta \times R^2}{(1/2)\Delta\theta_0 \times R^2} = \frac{\Delta\theta}{\theta_0} \quad (1)$$

where θ_0 = 45° is the rotating angle from the fully contacted position to the adjacent fully separated position, and A_0 is the maximum separated area for one sector. Then we can get

$$\Delta\sigma = \sigma_0 \times \frac{\Delta\theta}{\theta_0} \quad (2)$$

These theoretical expectations were further confirmed by electrical output measurements of the open-circuit voltage (V_{OC}), transferred charge density ($\Delta\sigma$), and short-circuit

dx.doi.org/10.1021/nl4013002 | Nano Lett. 2013, 13, 2916–2923

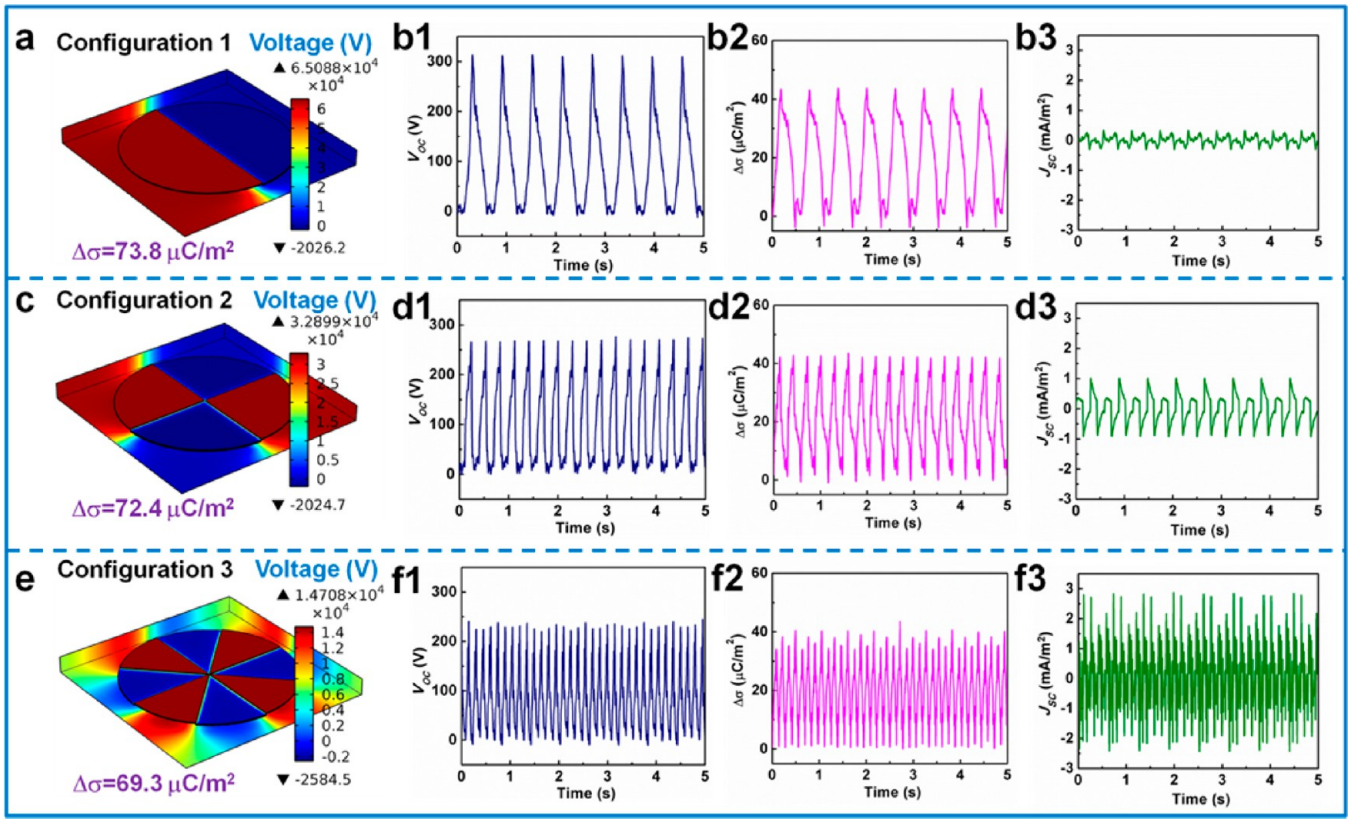

Figure 3. Configuration dependence of the output performance of the disk TENG. (a) The calculated open-circuit voltage and transferred charge density for the disk TENG with Configuration 1, in which the whole disk was divided into one sector (half of the full round shape). (b) The measured (b1) open-circuit voltage, (b2) transferred charge density, and (b3) short-circuit current density of Configuration 1 at 100 rpm. (c) The calculated open-circuit voltage and transferred charge density for the disk TENG with Configuration 2, in which the whole disk was divided into two sectors. (d) The measured (d1) open-circuit voltage, (d2) transferred charge density, and (d3) short-circuit current density of Configuration 2 at 100 rpm. (e) The calculated open-circuit voltage and transferred charge density for the disk TENG with Configuration 3, in which the whole disk was divided into four sectors (equivalent to the structure discussed in Figures 1 and 2). (f) The measured (f1) open-circuit voltage, (f2) transferred charge density, and (f3) short-circuit current density of Configuration 3 at 100 rpm.

current density (J_{SC}), as shown in Figure 2c–e. The measurement was accomplished by rotating the Al-side disk at a constant speed of 45 rpm, with vertically intimate contact with the inner surface of Kapton (the detailed measurement setup is described in Methods). The output profiles of both the V_{OC} and the $\Delta\sigma$ show excellent consistency with the calculation results, with the V_{OC} showing a sharp peak and the $\Delta\sigma$ showing a linear "triangle waveform" behavior. Based on eq 2, the dependence of J_{SC} on the angular speed (ω) can be deduced as:

$$J_{SC} = \frac{d(\Delta\sigma)}{dt} = \frac{d}{dt}\left(\sigma_0 \times \frac{\Delta\theta}{\theta_0}\right) = \frac{\sigma_0}{\theta_0}\frac{d(\Delta\theta)}{dt} = \frac{\sigma_0\omega}{\theta_0} = \frac{\sigma_0}{\theta_0} \times 2\pi \times \frac{n}{60} \quad (3)$$

where n is the rotation speed measured in a unit of rounds per minute (rpm). Therefore, as long as the angular speed (ω) remains constant, the J_{SC} should remain a constant value in each half cycle, with a symmetric AC manner in a full cycle. The measurement result of the J_{SC} in Figure 2e is also in agreement with this anticipated trend, which shows a "square waveform" behavior, differing a lot from the "pulse-like" current peak behavior in the previous works. This novel characteristic of NG's output performance may bring up new applications in various fields.

The disk TENG we discussed here is based on the triboelectrification between an insulator and a conductor (metal). If such disk TENGs are constructed based on the triboelectrification between two insulators as shown in Figure S2, they still work well under the similar rotation-induced in-plane charge separation mechanism, only except that the triboelectric charges on both the contacting surfaces are static, and the electrons transfer would occur between the two electrodes deposited on the back sides of the two insulator materials.

The electricity generation process of the disk TENG relies on the magnitude and the rate of the triboelectric charge separation. In this regard, the configuration of the device, which is the number of sectors (N) that the entire disk is divided into, can be expected to play a significant role in the output performance of the TENG. For this purpose, we studied three types of TENG devices with the disks divided into 1 sector (Configuration 1, semicircle), 2 sectors (Configuration 2), and 4 sectors (Configuration 3, equivalent to the structure discussed in Figures 1 and 2), respectively. Both theoretical calculations and measurements (with a rotation speed of 100 rpm) were carried out to demonstrate the effect of configurations on the output performance, as given in Figure 3. From the numerical calculation results in Figure 3a, c, and e, it could be found that as N increases from 1 to 4, both the calculated potential difference and transferred charge density

dx.doi.org/10.1021/nl4013002 | Nano Lett. 2013, 13, 2916–2923

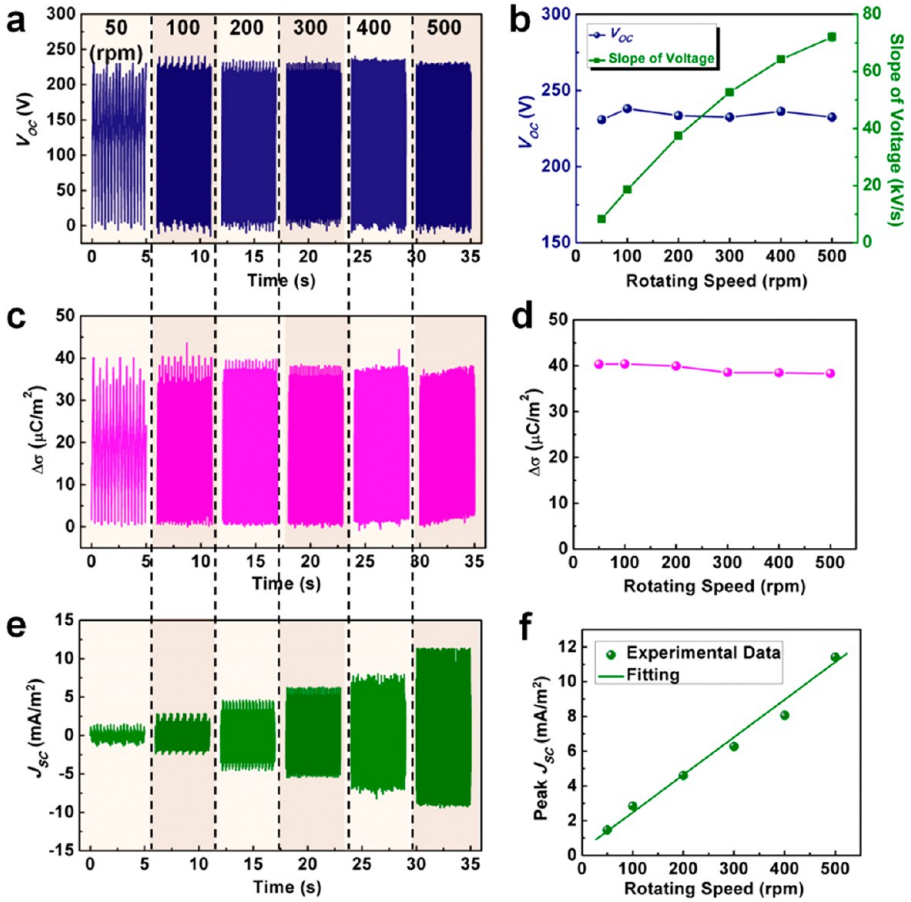

Figure 4. Influence of the rotating speed on the output performance of the disk TENG. (a) The measured open-circuit voltage with different rotating speeds from 50 to 500 rpm. (b) The summarized relationship between the open-circuit voltage/slope of the voltage and the rotating speed. (c) The measured transferred charge density with different rotating speeds from 50 to 500 rpm. (d) The summarized relationship between the transferred charge density and the rotating speed. (e) The measured short-circuit current density with different rotating speeds from 50 to 500 rpm. (f) The summarized relationship between the short-circuit current density and the rotating speed.

drop to some extent. This trend is also observed in the measurement results of the V_{OC} and the $\Delta\sigma$ (Figure 3b,d,f), in which the V_{OC} falls from 315 to 230 V, and the $\Delta\sigma$ decreases slightly from 43.6 to 40.8 $\mu C/m^2$. The decreases of the V_{OC} and the $\Delta\sigma$ may result from the lower magnitude of polarization due to the shrunk separation distance for finer segments. On the contrary, the J_{SC} shows a phenomenal ascending trend from Configuration 1 to Configuration 3, mainly owing to the obvious increasing of the charge transferring rate due to the smaller rotation angle from fully contact to fully separation. Above all, it could also be found that the frequencies of all the three types of output signals double with the doubled segmentations. To be more accurate, each frequency of the output signal was examined and summarized in Table S1, and the experimental results fit well with the theoretical calculations on the basis of the following equation:

$$f = \frac{n}{60} \times N \tag{4}$$

where n is the rotating speed and N is the number of divided sectors in a device. This group of comparisons shows a clear trend that ,with finer segmentation patterns, the amount of electricity generated by the TENG within a single rotation cycle will be largely increased owing to the multiple times (N) of charge transferred across the external load, which can greatly boost up the power conversion efficiency. Based on this finding, through patterning the disk with much finer segmentations using the techniques of photolithography and etching in the future work, the current output could be greatly improved.

On the other hand, when there is no segmentation but just two full-round-shaped disks, the output will be much lower: 8 V, 1.2 $\mu C/m^2$, and 1.5 $\mu A/m^2$ as the values of V_{OC}, $\Delta\sigma$, and J_{SC}, respectively, at a rotating speed of 100 rpm (Figure S3), which are about 2 orders of magnitude lower than the results in Figure 3. Ideally, if the contacting surfaces were perfectly flat and there were no wobbling during the rotation, there should be no electric output for this case. The observed electric output is likely due to the roughness of the two disk surfaces, which causes a fluctuation in contact area in the vertical direction.

Besides, an intimate contact in the vertical direction is also highly desired in the current proposed mechanism. To elucidate this issue, another set of experiments was carried out with a series of vertical distances between the pair of concentric disks of Configuration 3, at the rotating speed of 100 rpm. It could be found in Figure S4 that the output performance will rapidly decay to zero as the vertical displacement between the two plates increases from 0 to 2 mm. These results provide us with the two important necessities for the high output of the disk TENG and offer a strong validation for the proposed in-plane charge-separation-based working mechanism of the TENG in this work.

dx.doi.org/10.1021/nl4013002 | *Nano Lett.* 2013, 13, 2916−2923

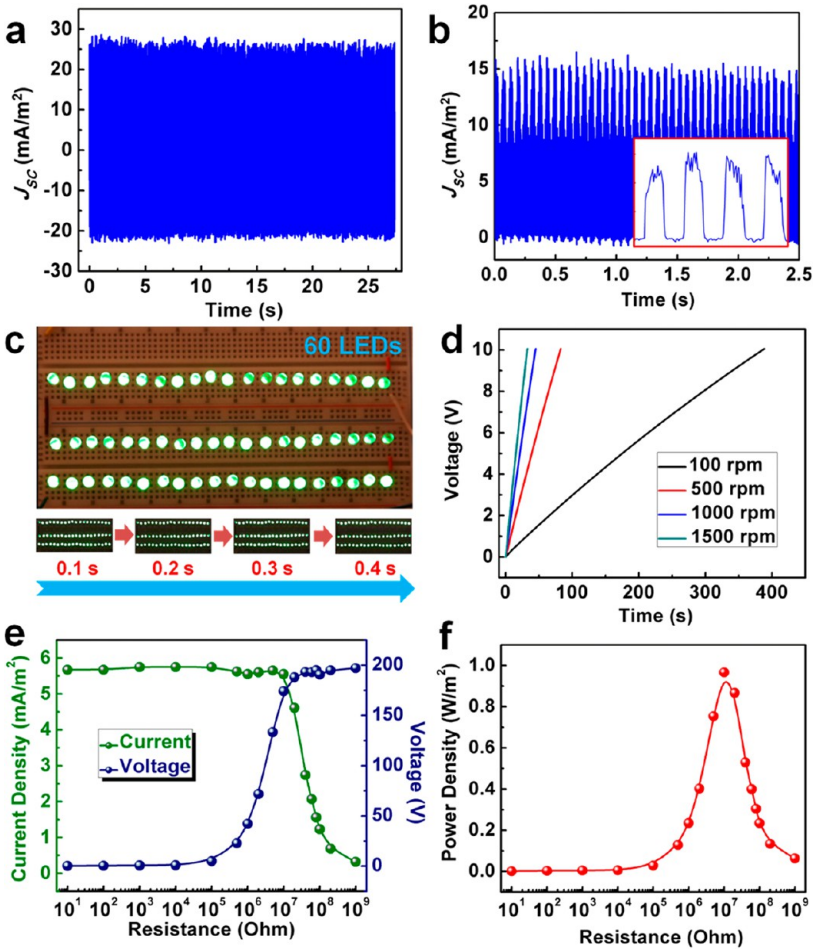

Figure 5. The disk TENG as a power source with high current output and frequency. (a) The measured output current for Configuration 3 at 1000 rpm. (b) The rectified output current for Configuration 3 at 1000 rpm. The inset is an enlarged view of the rectified output current with "square waveform" output profile. (c) Top: a snapshot showing the instantaneous and continuous powering of 60 green LEDs in series by the disk TENG working at 1000 rpm. Bottom: four consecutive frames captured from Video S1 with the time interval of 0.1 s. (d) The measured voltage of a 22 μF capacitor charged by the disk-TENG at variable rotating speeds. (e) The relationship between the output voltage/current and the resistance of an external load. (f) The relationship between the effective power density and the resistance of the external load. The maximum power is received when the external resistance is 10 MΩ.

As we have discussed in the theoretical analysis, the J_{SC} will increase linearly with the rotating speed n, while the V_{OC} and the $\Delta\sigma$ should not be influenced by the velocity, as long as the configuration of the device is fixed and the initial surface charge density keeps constant (eq 3). To verify these relationships, a group of electrical measurements with variable rotating speeds were conducted on the TENG with Configuration 3, which is presented in Figure 4. Figure 4a and c shows the measured open-circuit voltage and transferred charge density with different rotating speeds. Both the V_{OC} and the $\Delta\sigma$ almost keep constant with the rotating speed increased from 50 to 500 rpm. Though a slight decay at high speed occurs, which might result from the relatively low sampling rate of the voltage/charge meter, it is negligible with the V_{OC} of around 230 V and $\Delta\sigma$ of about 40 μC/m^2, as summarized in Figure 2b and d. Besides, the averaged slopes of the V_{OC} curve were also analyzed and shown in Figure 4b, with an increasing trend with ascending rotating speed because of the rising of the charge separation rate. Different from the V_{OC} and the $\Delta\sigma$, the J_{SC} is strongly enhanced with higher rotating speed (Figure 4e), and the good linear fitting in Figure 4f is coherently consistent with the behavior predicted by eq 3. This linear relationship between the J_{SC} and the rotating speed implies that the magnitude of the output current of the disk TENG could be utilized to actively measure the angular speed of a rotating disk structure, which has potential applications in automobile braking systems or transmitting instruments.

Moreover, though the magnitude of both the V_{OC} and the $\Delta\sigma$ is independent of the rotating speed, their frequencies, as well as the frequency of the J_{SC} will be directly related to the velocity (eq 4). Figure S5 summarizes the velocity dependence of the signal frequencies for V_{OC}, $\Delta\sigma$, and J_{SC}. It is obvious that the frequencies of all the three output signals show similar linear relationship with the rotating speed, and the frequency–velocity dependence also fits perfectly to the theoretically calculated curve, as shown in Figure S5d. The frequency analysis provides another reliable approach of employing the disk TENG as a self-powered velocity sensor. In the practical application, this could be simply realized by Fourier transform of any output signal to acquire the frequency information.

This unique design of the segmentally patterned disk TENG realizes multiple times of charge transfers within a full rotation cycle, which enables a fast charge transfer rate at high rotating speed. This will contribute to a large output current at a high

dx.doi.org/10.1021/nl4013002 | Nano Lett. 2013, 13, 2916–2923

frequency. The current output of the demonstrated disk TENG at 1000 rpm could reach 29.0 mA/m^2 (Figure 5a), corresponding to 117.6 μA for the entire device area of 40.54 cm^2. The frequency of the J_{SC} is as high as ~66.7 Hz, which is even a bit higher than the frequency of the commercial electric power (50 Hz). After rectification, a high-magnitude and high-frequency DC like output was achieved (Figure 5b), which can be used to drive portable electronic devices (e.g., 60 serially connected commercial LEDs) instantaneously, as shown in Figure 5c and Videos S1−2. As we can see from four consecutive frames in Figure 5c (with a time interval of only 0.1 s) taken from Video S1, the disk TENG achieves a continuous lighting-up of the LEDs, rather than just flashing in previous works.[17−19] Besides, such high frequency and large magnitude of electrical output imply a large averaged output current density and power density, which also shows its superiority when combined with energy storage units (e.g., batteries and capacitors) for long-term applications. As shown in Figure 5d, a 22 μF capacitor was charged by the disk TENG with variable rotating speeds at 100, 500, 1000, and 1500 rpm. The capacitor charging rates (the rate of the capacitor's voltage increase) rose almost linearly with the rotating speed (Figure S6) because of the faster charge transfer under higher rotation speeds. With the highest tested rotation rate at 1500 rpm using the device we have fabricated, the 22 μF capacitor was charged to 10 V in merely 33 s, which is a gigantic enhancement compared to the previous work[17] using the traditional type of TENG. The ultrafast charging of an energy storage unit by the disk TENG will largely improve the practicability of the TENG as an energy harvester in a self-powered system[27] and boost up the advancement of self-charging power cell.[28]

For different practical applications, the energy harvester is usually applied on external loads with variable resistances, so that the output will deviate from the short-circuit or open-circuit conditions. In this regard, the output performance of the disk TENG was systematically studied at different loads. Figure 5e shows the resistance dependence of both output current density and voltage, from 10 Ω to 1 GΩ. The output current density decreases with the increasing resistance while the output voltage shows the reverse trend, but both the current and voltage tend to saturate at both high and low ends of the resistance. The power density was also calculated by:

$$\frac{P}{A} = U \times \frac{I}{A} = UJ \tag{5}$$

where P is the output power, A is the surface area of one disk unit in the TENG, U and I are the voltage and the current on the load with a certain resistance, respectively, and J is the current density. The power density was also plotted as a function of external resistance in Figure 5f. The output power density first increases at a low resistance region and then decreases at a higher resistance region. The maximum value of the power density of ~1 W/m^2 occurs at ~10 MΩ.

The disk TENG based on in-plane charge separation process has several advantages over the TENG based on vertical-to-plane charge separation process. First, this novel working mode enables the energy harvesting from rotational motion, which largely broadens the range of applications of TENGs for a range of centric types of motion. Second, such continuous-motion-driven TENG generates the electricity with adjustable frequency and at high frequency, because it does not rely on the resilient bouncing of the TENG after mechanical triggering. This could help to realize a direct and continuous driving of electronic devices and fast charging of storage units. Third, the in-plane charge separation does not require the presence of an air gap, making the TENG device more suitable for multilayer integration and fully packaging. Last but not least, with the innovative design of device configuration, this is the first to realize the nanogenerator working at constant velocity of rotation, and a reliable self-powered angular speed sensor could be obtained.

In summary, we present a novel design of disk-shaped triboelectric nanogenerator based on in-plane charge separation mechanism, which can convert rotational mechanical energy into electricity. Finite element simulation was employed to gain a comprehensive understanding about the fundamental working principle as well as the output characteristics of the TENG, and the experimental results are in good agreement with the theoretical predictions. Through experimental comparison, we find an enhancement of the output current from finer segmental patterns, which can serve as the guidance for future research on the disk TENG. A linear relationship is present between the current/frequency and the rotating speed, which enables its application as a self-powered angular speed sensor. The disk TENG makes it possible to harvest rotational mechanical energy at a high frequency with a high magnitude of power density, showing unprecedented superiority and practicability in both driving electronic devices directly and continuously as well as charging energy storage units. This work opens up a new field in mechanical energy harvesting and pushes forward a significant step toward the practical application of nanogenerators by using rotary motion, such as the brake system in an automobile.

Methods Summary. *Fabrication of the Kapton Nanorods.* A 50-μm-thick Kapton thin film was cleaned with menthol, isopropyl alcohol, and deionized water, consecutively, and then blown dry with nitrogen gas. Then, the surface of the Kapton was deposited with a 10 nm Au thin film by sputtering as the mask for the following etching of the Kapton surface to create the nanorod structure using the inductively coupled plasma (ICP) reactive ion etching. Specifically, Ar, O_2, and CF_4 gases were introduced into the ICP chamber with the flow rate of 15.0, 10.0, and 30.0 sccm, respectively. One power source of 400 W was used to generate a large density of plasma, and the other power of 100 W was used to accelerate the plasma ions. The Kapton thin film was etched for 1−5 min, and the length of the as-fabricated nanorod array ranged from 0.4 to 1.1 μm.

Fabrication of the Disk Triboelectric Nanogenerator. First, two 0.125″-thick PMMA sheets were processed by laser cutting (PLS6.75, Universal Laser Systems) to form the two cyclostyles with the same shape as the corresponding configuration. The tailored Al foil and Kapton film (deposited with Au electrode) were securely attached on the PMMA loading templates to make a flat surface. The two sheets were put together with the two fresh surface (Al and Kapton) intimately contacted.

Electrical Output Measurement of the Disk-Triboelectric Nanogenerator. In the electrical output measurement, the Al part of the disk-triboelectric nanogenerator was bonded onto a spinning motor (BX460AM-A, Oriental Motor), and the Kapton part was secured on a stationary XYZ linear translation stage (462-XYZ-M, Newport Incorporation), with both centers of the disks in coincidence with the spinning axis. The Al structure was driven to rotate around the axis of the motor with variable rotating speeds. The open-circuit voltage and transferred charge density was measured by Keithley 6514 system

electrometer, and the short-circuit current was measured by SR570 low noise current amplifier (Stanford Research System).

■ ASSOCIATED CONTENT

Supporting Information

More detailed information about the morphology of the Kapton nanorods, the disk TENGs based two insulator materials, the output frequencies of the disk TENGs with different configurations, control experiments, the output frequencies under different rotating speeds, the summary of the capacitor charging rates, as well as the videos of instantaneously and continuously driving LEDs. This material is available free of charge via the Internet at http://pubs.acs.org.

■ AUTHOR INFORMATION

Corresponding Author

*E-mail: zlwang@gatech.edu.

Author Contributions

L.L. and S.W. contributed equally to this work.

Notes

The authors declare no competing financial interest.

■ ACKNOWLEDGMENTS

Research was supported by the U.S. Airforce, U.S. Department of Energy, Office of Basic Energy Sciences (Award DE-FG02-07ER46394), NSF (0946418), and the Knowledge Innovation Program of the Chinese Academy of Science (Grant No. KJCX2-YW-M13). Patents have been filed based on the research results presented in this manuscript.

■ REFERENCES

(1) Beeby, S. P.; Tudor, M. J.; White, N. M. *Meas. Sci. Technol.* **2006**, *17*, R175−R195.
(2) Mitcheson, P. D.; Yeatman, E. M.; Rao, G. K.; Holmes, A. S.; Green, T. C. *Proc. IEEE* **2008**, *96*, 1457−1486.
(3) Wang, Z. L.; Wu, W. Z. *Angew. Chem., Int. Ed.* **2012**, *51*, 11700−11721.
(4) Wang, Z. L.; Zhu, G.; Yang, Y.; Wang, S. H.; Pan, C. F. *Mater. Today* **2012**, *15*, 532−543.
(5) Wang, Z. L.; Song, J. H. *Science* **2006**, *312*, 242−246.
(6) Qin, Y.; Wang, X. D.; Wang, Z. L. *Nature* **2008**, *451*, 809−U805.
(7) Chang, C. E.; Tran, V. H.; Wang, J. B.; Fuh, Y. K.; Lin, L. W. *Nano Lett.* **2010**, *10*, 726−731.
(8) Chen, X.; Xu, S. Y.; Yao, N.; Shi, Y. *Nano Lett.* **2010**, *10*, 2133−2137.
(9) Hu, Y. F.; Lin, L.; Zhang, Y.; Wang, Z. L. *Adv. Mater.* **2012**, *24*, 110.
(10) Williams, C. B.; Shearwood, C.; Harradine, M. A.; Mellor, P. H.; Birch, T. S.; Yates, R. B. *Proc. IEEE Circ. Dev. Syst.* **2001**, *148*, 337−342.
(11) Beeby, S. P.; Torah, R. N.; Tudor, M. J.; Glynne-Jones, P.; O'Donnell, T.; Saha, C. R.; Roy, S. *J. Micromech. Microeng.* **2007**, *17*, 1257−1265.
(12) Mitcheson, P. D.; Miao, P.; Stark, B. H.; Yeatman, E. M.; Holmes, A. S.; Green, T. C. *Sens. Actuators A* **2004**, *115*, 523−529.
(13) Naruse, Y.; Matsubara, N.; Mabuchi, K.; Izumi, M.; Suzuki, S. *J. Micromech. Microeng.* **2009**, 19.
(14) Fan, F. R.; Tian, Z. Q.; Wang, Z. L. *Nano Energy* **2012**, *1*, 328−334.
(15) Fan, F. R.; Lin, L.; Zhu, G.; Wu, W. Z.; Zhang, R.; Wang, Z. L. *Nano Lett.* **2012**, *12*, 3109−3114.
(16) Zhu, G.; Pan, C. F.; Guo, W. X.; Chen, C. Y.; Zhou, Y. S.; Yu, R. M.; Wang, Z. L. *Nano Lett.* **2012**, *12*, 4960−4965.
(17) Wang, S. H.; Lin, L.; Wang, Z. L. *Nano Lett.* **2012**, *12*, 6339−6346.
(18) Zhang, X. S.; Han, M. D.; Wang, R. X.; Zhu, F. Y.; Li, Z. H.; Wang, W.; Zhang, H. X. *Nano Lett.* **2013**, *13*, 1168−1172.
(19) Zhu, G.; Lin, Z. H.; Jing, Q. S.; Bai, P.; Pan, C. F.; Yang, Y.; Zhou, Y. S.; Wang, Z. L. *Nano Lett.* **2013**, *13*, 847−853.
(20) Yang, Y.; Lin, L.; Zhang, Y.; Jing, Q. S.; Hou, T. C.; Wang, Z. L. *ACS Nano* **2012**, *6*, 10378−10383.
(21) Castle, G. S. P. *J. Electrostat.* **1997**, *40*−*41*, 13−20.
(22) McCarty, L. S.; Whitesides, G. M. *Angew. Chem., Int. Ed.* **2008**, *47*, 2188−2207.
(23) Wiles, J. A.; Grzybowski, B. A.; Winkleman, A.; Whitesides, G. M. *Anal. Chem.* **2003**, *75*, 4859−4867.
(24) Wang, S. H.; Lin, L.; Xie, Y. N.; Jing, Q. S.; Niu, S. M.; Wang, Z. L. *Nano Lett.* **2013**, DOI: 10.1021/nl400738p.
(25) Zhu, G.; Chen, J.; Liu, Y.; Bai, P.; Zhou, Y. S.; Jing, Q. S.; Pan, C. F.; Wang, Z. L. *Nano Lett.* **2013**, DOI: 10.1021/nl4008985.
(26) Fang, H.; Wu, W. Z.; Song, J. H.; Wang, Z. L. *J. Phys. Chem. C* **2009**, *113*, 16571−16574.
(27) Hu, Y. F.; Zhang, Y.; Xu, C.; Lin, L.; Snyder, R. L.; Wang, Z. L. *Nano Lett.* **2011**, *11*, 2572−2577.
(28) Xue, X. Y.; Wang, S. H.; Guo, W. X.; Zhang, Y.; Wang, Z. L. *Nano Lett.* **2012**, *12*, 5048−5054.